Journal of Non-Newtonian Fluid Mechanics 204 (2014) 50–61

Contents lists available at ScienceDirect

Journal of Non-Newtonian Fluid Mechanics

journal homepage: http://www.elsevier.com/locate/jnnfm

Numerical solution of the FENE-CR model in complex flows

G.S. Paulo [a], C.M. Oishi [a], M.F. Tomé [b,*], M.A. Alves [c], F.T. Pinho [d]

[a] Departamento de Matemática e Computação, Universidade Estadual Paulista "Júlio de Mesquita Filho", Rua Roberto Simonsen, 305, 19060-900 Presidente Prudente, Brazil
[b] Departamento de Matemática Aplicada e Estatística, Universidade de São Paulo, Av. Trabalhador São-carlense, 400 – Centro, São Carlos, Brazil
[c] Departamento de Engenharia Química, Centro de Estudos de Fenómenos de Transporte, Faculdade de Engenharia da Universidade do Porto, Rua Dr. Roberto Frias s/n, 4200-465 Porto, Portugal
[d] Departamento de Engenharia Mecânica, Centro de Estudos de Fenómenos de Transporte, Faculdade de Engenharia da Universidade do Porto, Rua Dr. Roberto Frias s/n, 4200-465 Porto, Portugal

ARTICLE INFO

Article history:
Received 31 July 2013
Received in revised form 18 November 2013
Accepted 20 November 2013
Available online 11 December 2013

Keywords:
FENE-CR model
Channel flow
Cross-slot geometry
Impacting drop
Free surface flows

ABSTRACT

A finite difference technique for solving the FENE-CR (Finite Extendable Non-linear Elastic – Chilcott and Rallison) closure constitutive model in complex flows has been developed and tested. The governing equations are solved using a Marker-and-Cell type method on a staggered grid. The momentum equation is integrated employing an implicit method while the FENE-CR constitutive equation is approximated by a second-order Runge–Kutta scheme. To demonstrate that the numerical technique can cope with complex flows governed by the FENE-CR model, three flow problems were analysed: the fully-developed channel flow, the 2D cross-slot flow and the impacting drop problem. The analytic solution for fully-developed channel flow of FENE-CR fluids with a solvent viscosity is also presented for validation purposes. This flow problem is used to verify the numerical method and to quantify its accuracy by comparing numerical results of fully-developed channel flow with the analytic solution. The second flow is employed to assess whether the numerical methodology is capable of capturing the purely-elastic instabilities predicted in the literature for 2D cross-slot confined flows. Additionally, the complex free surface flow corresponding to the filling of a 2D cross geometry has also been investigated. The last problem concerns the flow dynamics of a FENE-CR fluid drop impacting on a rigid surface, which allows the assessment of the capability of the model to deal with free surfaces. The effects of varying the Reynolds number, the Weissenberg number and the finite extensibility of the polymer molecules (L^2) on the resulting flow patterns are analysed.

1. Introduction

Problems involving deformation of viscoelastic fluids in complex flow configurations are important in many applications, including ink-jet printing devices, extrusion flows, filament stretching, contraction flows and cross-slot flows. Therefore, there is an industrial interest in accurately predicting complex flows, and a variety of numerical techniques for simulating viscoelastic fluid flows have been proposed over the years by many researchers. Among the differential constitutive models studied, the Oldroyd-B, Upper-Convected Maxwell (UCM), Phan–Thien–Tanner (PTT), eXtended Pom–Pom (XPP), FENE-CR, FENE-P and Giesekus models have been investigated (e.g. see [1–7]). The problems investigated include the jet buckling and impacting drop [1–9], extrudate swell [9,10], cross-slot flow [5,11–14], contraction flows [4], among others.

In this work, we are concerned with two-dimensional (2D) numerical simulations of viscoelastic flows described by the FENE-CR constitutive equation with a Newtonian solvent contribution. We deal specifically with three benchmark problems: fully-developed flow in a channel [15–17], flow in a cross-slot geometry [11–14] and the impacting drop problem [1–3,6–8]. The cross-slot geometry has been employed for extensional rheology measurements and, more recently, to investigate purely-elastic flow instabilities of viscoelastic fluids. Gardner et al. [18] presented experimental results showing the onset of an elastic instability in the cross-slot flow problem. Arratia et al. [19] turned back to this problem and reported two different types of elastic instabilities in a microfluidic cross-slot geometry. In the first instability the flow became deformed and asymmetric, but remained steady and a second instability, characterized by the transition to an unsteady flow with non-periodic fluctuations, was observed at higher strain rates. Poole et al. [13] used a numerical technique to solve the UCM constitutive equation and successfully predicted the steady

* Corresponding author. Tel.: +55 1633739656; fax: +55 1633739650.
E-mail addresses: gilcilene@fct.unesp.br (G.S. Paulo), cassiooishi@gmail.com (C.M. Oishi), murilo@icmc.usp.br (M.F. Tomé), mmalves@fe.up.pt (M.A. Alves), fpinho@fe.up.pt (F.T. Pinho).

0377-0257/$ - see front matter © 2013 Elsevier B.V. All rights reserved.
http://dx.doi.org/10.1016/j.jnnfm.2013.11.003

asymmetry under creeping flow conditions resulting from the first instability. They also showed that inertia reduces the magnitude of the asymmetry and promotes flow stability, while at Reynolds numbers (Re) of $Re = 0.01$ and 0.1 the flow dynamics was essentially similar to that found under creeping flow conditions. More recently, Rocha et al. [14] extended the previous studies using infinitely extensionable models (UCM and Oldroyd-B fluids) to finite extendable non-linear elastic models (FENE-P and FENE-CR models) and provided quantitative data for flows in planar cross-slot geometries with sharp and rounded corners. The effects of finite extensibility of the model dumbbell, Weissenberg number (Wi) and concentration of polymer solution on the flow were numerically analysed. The loss of flow symmetry caused by the instability in the cross-slot geometry was identified recently by Wilson [20] as one open problem in the mathematical modeling of the flow of non-Newtonian fluids. According to Wilson [20], numerical and analytical works addressing predictions of the corresponding linear instability beyond the bifurcation point are scarce. Therefore, it is worth to study further this problem both numerically and theoretically. In this work, we examine the first kind of instability employing a different numerical technique from that used by Rocha et al. [14] and we also investigate whether our method can qualitatively and quantitatively predict the same flow instabilities. Furthermore, in order to demonstrate the ability of the numerical code to solve viscoelastic free surface flows, we solve the filling of the cross-slot geometry, which involves the progression of a free surface boundary.

In the context of viscoelastic free surface flows, the impacting drop problem has been studied by a number of researchers. Numerical simulations of the impacting drop problem using the finite difference method (FDM) and the front-tracking technique were presented by Tomé et al. [2] and Oishi et al. [7]. In the former, the authors investigated the viscoelastic behavior of the Oldroyd-B model while the latter analysed the influence of the various rheological parameters that characterize the XPP fluid. By using the smoothed particle hydrodynamics (SPH) methodology, Fang et al. [3] and Rafiee et al. [6] studied this free surface flow numerically using an Oldroyd-B fluid. Recently, Jiang et al. [8] compared FDM and SPH methods applied to simulate an Oldroyd-B drop impact and spreading on a rigid wall, while Jiang et al. [1] simulated the viscoelastic drop impact of a XPP fluid using an improved SPH method.

In this work, we present a finite difference technique for simulating two-dimensional flows described by the FENE-CR model with a Newtonian solvent contribution and apply the methodology to investigate the cross-slot flow and the drop impact problems. Firstly, to verify the numerical technique, an analytic solution for fully-developed channel flow is derived and used to confirm the correctness and accuracy of the numerical code employed to solve fully-developed flow. In the first application, by assuming low Re flow conditions, a range of L^2 and Wi values is studied for five meshes with different refinement levels. Secondly, varying Re and Wi, we investigated the influence of the extensibility parameter L^2 on the spreading of a FENE-CR fluid drop. Although other codes have been developed to solve these problems, detailed numerical studies, considering, for example, refined meshes and the influence of the rheological parameters that characterize the FENE-CR model, have received relatively little attention. Therefore, we expect that the results of this paper can be used not only to test numerical methods but also to benefit the understanding of rheological behavior on the cross-slot flow and the drop impact problems.

The remaining of this paper is organized as follows: in Section 2, the governing equations, boundary conditions and details of the numerical method are presented. Section 3 provides a verification of the methodology by simulating viscoelastic free surface flows in a channel and in Section 4, numerical results obtained in the simulation of planar cross-slot and impacting drop problems are presented and discussed. Conclusions are summarized in Section 5. The derivation of the analytic solution for fully-developed flow of FENE-CR fluid with a Newtonian solvent contribution is detailed in Appendix A.

2. Mathematical formulation

The system of dimensionless equations representing isothermal, incompressible, viscoelastic flows governed by the FENE-CR constitutive equation can be described as:

$$\nabla \cdot \mathbf{u} = 0, \tag{1}$$

$$\frac{\partial \mathbf{u}}{\partial t} = -\nabla \cdot (\mathbf{uu}) - \nabla p + \frac{\beta}{Re}\nabla^2 \mathbf{u} + \nabla \cdot \boldsymbol{\tau} + \frac{1}{Fr^2}\mathbf{g}, \tag{2}$$

$$\boldsymbol{\tau} = \frac{(1-\beta)}{ReWi} f(\mathrm{tr}(\mathbf{A}))(\mathbf{A} - \mathbf{I}), \tag{3}$$

$$\frac{\partial \mathbf{A}}{\partial t} = -\nabla \cdot (\mathbf{uA}) + \mathbf{A} \cdot \nabla \mathbf{u} + (\nabla \mathbf{u})^T \cdot \mathbf{A} - \frac{1}{Wi} f(\mathrm{tr}(\mathbf{A}))(\mathbf{A} - \mathbf{I}), \tag{4}$$

where t is the time, $\mathbf{u}$ is the velocity vector, p is the pressure, $\mathbf{g}$ is the gravitational field, and $\boldsymbol{\tau}$ and $\mathbf{A}$ are the extra-stress and conformation tensors, respectively. The dimensionless quantities $Fr = \frac{U}{\sqrt{gH}}$, $Re = \frac{\rho UH}{\eta_0}$, $Wi = \lambda \frac{U}{H}$ are the Froude, the Reynolds and the Weissenberg numbers, respectively, where H and U denote characteristic length and velocity scalings for each problem, g and ρ are the acceleration of gravity and fluid density, respectively, and λ is the fluid relaxation time. The amount of Newtonian solvent is controlled by the dimensionless solvent viscosity coefficient, $\beta = \frac{\eta_S}{\eta_0}$, where $\eta_0 = \eta_S + \eta_P$ denotes the total shear viscosity; η_S and η_P represent the Newtonian solvent and polymeric viscosities, respectively. The function f depends on the trace of $\mathbf{A}$, according to

$$f(\mathrm{tr}(\mathbf{A})) = \frac{L^2}{L^2 - \mathrm{tr}(\mathbf{A})}. \tag{5}$$

We note that the non-Newtonian extra-stress tensor and the pressure were normalized as $\boldsymbol{\tau} = \boldsymbol{\tau}^*/\rho U^2$ and $p = p^*/\rho U^2$, where the variables with a star are in dimensional form (most authors alternatively use the form $\boldsymbol{\tau} = \boldsymbol{\tau}^*/(\eta_0 U/H)$ and $p = p^*/(\eta_0 U/H)$).

To obtain a solution of the previous system of equations, it is necessary to specify appropriate initial and boundary conditions, which are described in the next section.

2.1. Initial and boundary conditions

We consider two-dimensional flows in a Cartesian coordinate system. The initial conditions for velocity and conformation tensor are $\mathbf{u} = \mathbf{0}$ and $\mathbf{A} = \mathbf{I}$, respectively.

On rigid boundaries, the no-slip condition ($\mathbf{u} = \mathbf{0}$) is employed for the momentum equation and for the constitutive equation the conformation tensor $\mathbf{A}$ is calculated directly from Eq. (4) similarly as was done in [22] for the polymer stress. The non-Newtonian tensor $\boldsymbol{\tau}$ is updated from Eq. (3).

At inlets, the normal velocity component is specified and the tangential velocity component is set to zero. On exits, the homogeneous Neumann condition is applied. The conformation tensor at the inlet is always consistent with the imposed velocity profile: if the velocity $\mathbf{u}$ is assumed uniform, then the conformation tensor is set as $\mathbf{A} = \mathbf{I}$; when a fully-developed parabolic velocity profile is used, the analytic expressions for the fully-developed components of the conformation tensor $\mathbf{A}$ are applied (see Appendix A).

On the fluid free surface, it is necessary to impose special boundary conditions for the velocity and pressure fields. We shall consider unsteady free-surface flows of a fluid moving into a

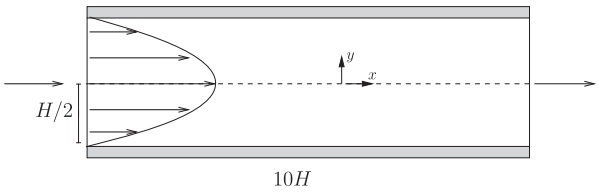

Fig. 1. Definition of the computational domain for 2D channel flow.

passive atmosphere (which we may take to be at zero relative pressure). In the absence of surface tension effects, the normal and tangential components of the total stress must be continuous across any free surface, so that on such a surface (see [21])

$$\mathbf{n}\cdot\boldsymbol{\sigma}\cdot\mathbf{n}^{\mathrm{T}}=0 \qquad \text{and} \qquad \mathbf{m}\cdot\boldsymbol{\sigma}\cdot\mathbf{n}^{\mathrm{T}}=0. \tag{6}$$

The total stress tensor is given by

$$\boldsymbol{\sigma}=-p\mathbf{I}+\boldsymbol{\tau}_{\mathrm{S}}+\boldsymbol{\tau}, \tag{7}$$

where $\boldsymbol{\tau}_{\mathrm{S}}=\frac{2\beta}{Re}\mathbf{D}$ is the Newtonian solvent contribution tensor and $\mathbf{D}=\frac{1}{2}[\nabla\mathbf{u}+(\nabla\mathbf{u})^{T}]$ is the rate of deformation tensor.

In Eq. (6), $\mathbf{n}$ represents a unit vector normal and external to the surface, and $\mathbf{m}$ is a unit vector tangent to the free surface. In the 2D flows investigated here it suffices to consider the two components $\mathbf{n}=(n_x,\ n_y)$ and $\mathbf{m}=(n_y,\ -n_x)$ in which case the stress conditions (6) can be written as

$$p=\beta\frac{2}{Re}\left[\frac{\partial u}{\partial x}n_x^2+\left(\frac{\partial u}{\partial y}+\frac{\partial v}{\partial x}\right)n_xn_y+\frac{\partial v}{\partial y}n_y^2\right]+\tau^{xx}n_x^2+2\tau^{xy}n_xn_y+\tau^{yy}n_y^2, \tag{8}$$

$$\frac{\beta}{Re}\left[2\left(\frac{\partial u}{\partial x}-\frac{\partial v}{\partial y}\right)n_xn_y+\left(\frac{\partial u}{\partial y}+\frac{\partial v}{\partial x}\right)\left(n_y^2-n_x^2\right)\right]+(\tau^{xx}-\tau^{yy})n_xn_y+\tau^{xy}\left(n_y^2-n_x^2\right)=0. \tag{9}$$

2.2. Details of the numerical method

The governing Eqs. (1)–(3) are solved by a MAC finite-difference method using the strategy of Oishi et al. [22], which combines the projection method with an implicit technique for the treatment of the pressure field on free surfaces. The GENSMAC (GENeralized Simplified Marker-And-Cell) [23] methodology is used to solve the momentum and the mass conservation equations on a staggered grid. More details about the classification of cells and discretization of the equations at the free surface can be found in [23].

The numerical method applied in this work is an adaptation of the algorithm proposed in [22] for solving viscoelastic free surface flows. In that paper, the authors employed the rheological equation formulated in terms of the extra-stress tensor for solving XPP fluid flows. Therefore, the methodology described in [22] will serve as a basis to implement the FENE-CR model represented in terms of the conformation tensor constitutive equation.

Firstly, we assume that at time $t=t_n$ the variables $\mathbf{u}(\mathbf{x},t_n)=\mathbf{u}^{(n)}, p(\mathbf{x},t_n)=p^{(n)},\ \boldsymbol{\tau}(\mathbf{x},t_n)=\boldsymbol{\tau}^{(n)}, \mathbf{A}(\mathbf{x},t_n)=\mathbf{A}^{(n)}$ and the markers' positions $\mathbf{x}(t_n)=\mathbf{x}^{(n)}$ are known. To update the solutions of these variables at $t=t_n+\delta t$, the following steps are solved:

Step 1: Obtain provisional values for the conformation $\mathbf{A}$ and extra-stress $\boldsymbol{\tau}$ tensors. For this purpose, the constitutive Eq. (4) is discretized using the second-order accuracy Runge–Kutta (RK21) method. Note that Eq. (4) can be written in the form

$$\frac{\partial\mathbf{A}}{\partial t}=\mathbf{F}(\mathbf{u},\mathbf{A}), \tag{10}$$

where

$$\mathbf{F}(\mathbf{u},\mathbf{A})=-\nabla\cdot(\mathbf{uA})+[\mathbf{A}\cdot\nabla\mathbf{u}+(\nabla\mathbf{u})^{T}\cdot\mathbf{A}]-\frac{1}{Wi}f(\mathrm{tr}(\mathbf{A}))[\mathbf{A}-\mathbf{I}]. \tag{11}$$

Now, by using the explicit forward Euler discretization in Eq. (10), we can compute the intermediate conformation tensor field $\widetilde{\mathbf{A}}^{(n+1)}$ by

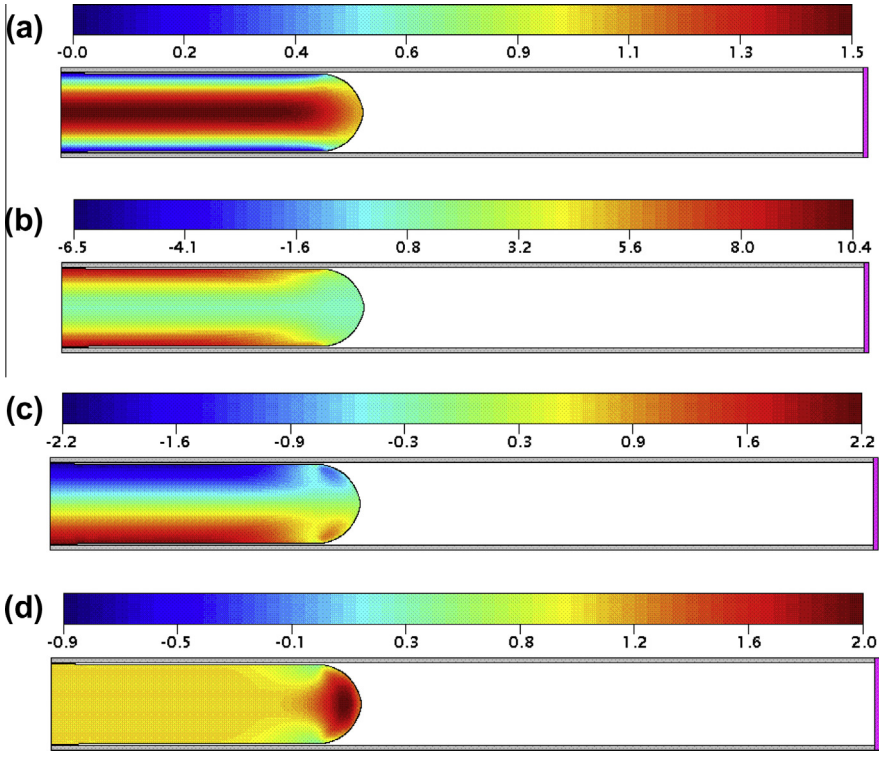

Fig. 2. Numerical results obtained at time $t=3.5$ on mesh $M50$. Profiles of the following variables: (a) u, (b) A^{xx}, (c) A^{xy} and (d) A^{yy}.

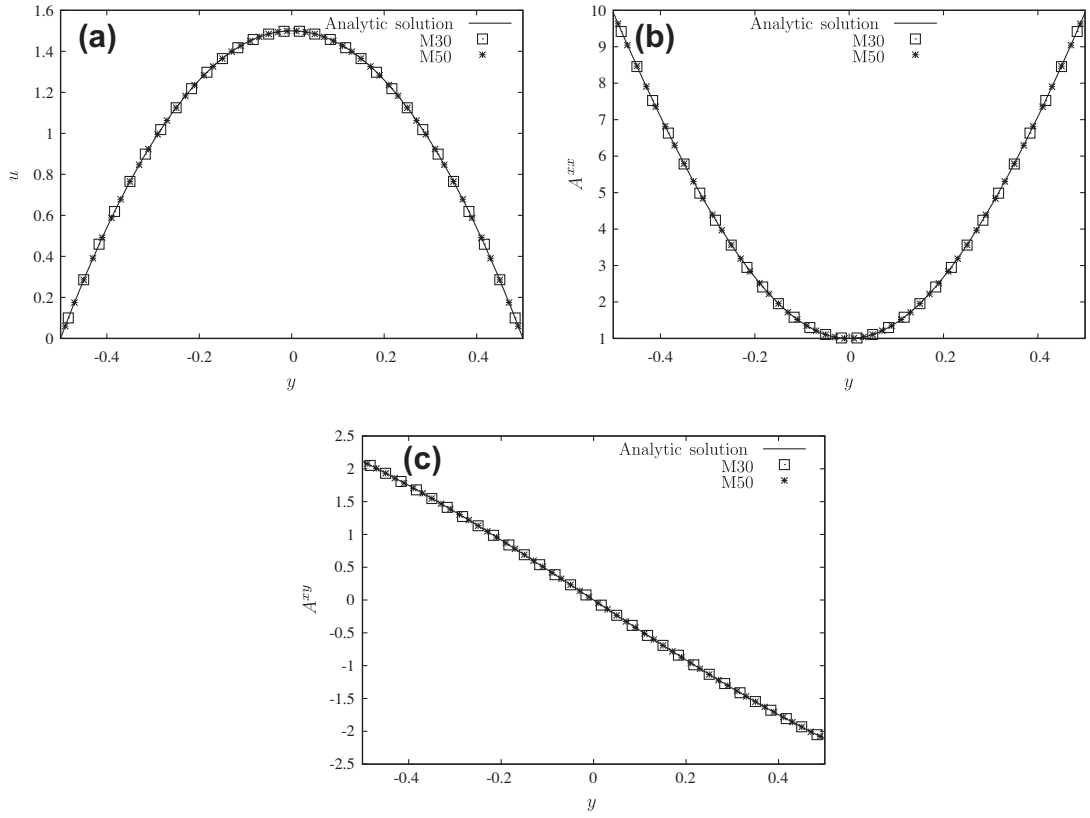

Fig. 3. Numerical and analytic solutions obtained at the middle of the channel of FENE-CR fluid flow using $Re = 0.2$, $Wi = 0.4$, $\beta = 0.3$ and $L^2 = 100$: (a) u, (b) A^{xx} and (c) A^{xy} at time $t = 50$ in the location $x^* = 5H$. The solid lines correspond to the exact solutions while the numerical solutions on meshes $M30$ and $M50$ are represented by symbols.

$$\widetilde{\mathbf{A}}^{(n+1)} = \mathbf{A}^{(n)} + \delta t \mathbf{F}(\mathbf{u}^{(n)}, \mathbf{A}^{(n)}). \tag{12}$$

Once $\widetilde{\mathbf{A}}^{(n+1)}$ is known, we calculate an intermediate non-Newtonian tensor $\tilde{\boldsymbol{\tau}}^{(n+1)}$ from Eq. (3), namely

$$\tilde{\boldsymbol{\tau}}^{(n+1)} = \frac{(1-\beta)}{ReWi} f(\mathrm{tr}(\widetilde{\mathbf{A}}^{(n+1)}))[\widetilde{\mathbf{A}}^{(n+1)} - \mathbf{I}]. \tag{13}$$

Step 2: Calculate a provisional velocity field $\tilde{\mathbf{u}}^{(n+1)}$. Following the ideas behind the projection method (see in [22]) to decouple the Navier–Stokes equations, the provisional velocity field $\tilde{\mathbf{u}}^{(n+1)}$ is obtained from Eq. (2). In this work we employ an implicit time discretization to calculate $\tilde{\mathbf{u}}^{(n+1)}$, i.e.,

$$\frac{\tilde{\mathbf{u}}^{(n+1)}}{\delta t} - \frac{\beta}{Re}\nabla^2\tilde{\mathbf{u}}^{(n+1)} = \frac{\mathbf{u}^{(n)}}{\delta t} - \nabla\cdot(\mathbf{uu})^{(n)} - \nabla p^{(n)} + \nabla\cdot\tilde{\boldsymbol{\tau}}^{(n+1)} + \frac{1}{Fr^2}\mathbf{g}, \tag{14}$$

where the boundary conditions for $\tilde{\mathbf{u}}^{(n+1)}$ are the same as those for the final velocity $\mathbf{u}^{(n+1)}$, to be determined below, and $p^{(n)}$ is an approximation to $p^{(n+1)}$.

Step 3: Solve the Poisson equation for the potential function ψ: it can be shown that the velocity field $\tilde{\mathbf{u}}^{(n+1)}$ possesses the correct vorticity at time t_{n+1} but it does not necessarily satisfy mass conservation [24]. Therefore, there exists a potential function ψ such that $\mathbf{u}^{(n+1)} = \tilde{\mathbf{u}}^{(n+1)} - \nabla\psi^{(n+1)}$ where, by enforcing continuity,

$$\nabla^2\psi^{(n+1)} = \nabla\cdot\tilde{\mathbf{u}}^{(n+1)}. \tag{15}$$

The boundary conditions required for solving this Poisson equation are the homogeneous Neumann conditions for rigid walls and inflows, while homogeneous Dirichlet conditions are applied at outflows. In order to maintain the stability of the numerical scheme applied to low Reynolds free surface flows, the implicit formulation proposed in [22] that derives equations for $\psi^{(n+1)}$ on the free surface, is employed. In generic form, these equations can be summarized as

Table 1
Relative errors calculated at the middle of the channel ($x = 5$) for each mesh employed.

Meshes	$E(u)$	$E(A^{xx})$	$E(A^{xy})$
$M20$	1.513e−03	5.483e−03	3.339e−03
$M30$	6.753e−04	2.443e−03	1.468e−03
$M40$	3.817e−04	1.376e−03	8.373e−04
$M50$	2.445e−04	8.814e−04	5.360e−04

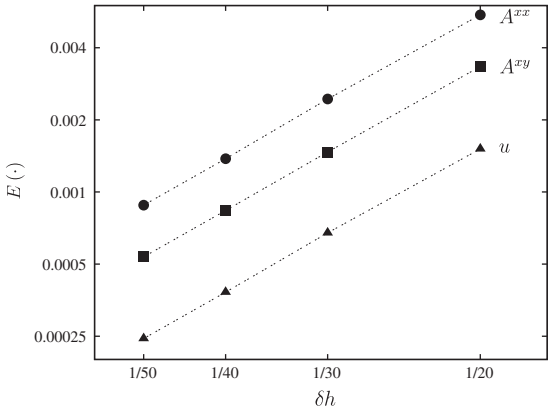

Fig. 4. Variation of the relative l_2-norm with mesh size (log–log scales) and lines of slope 2 illustrating second-order convergence of the numerical method.

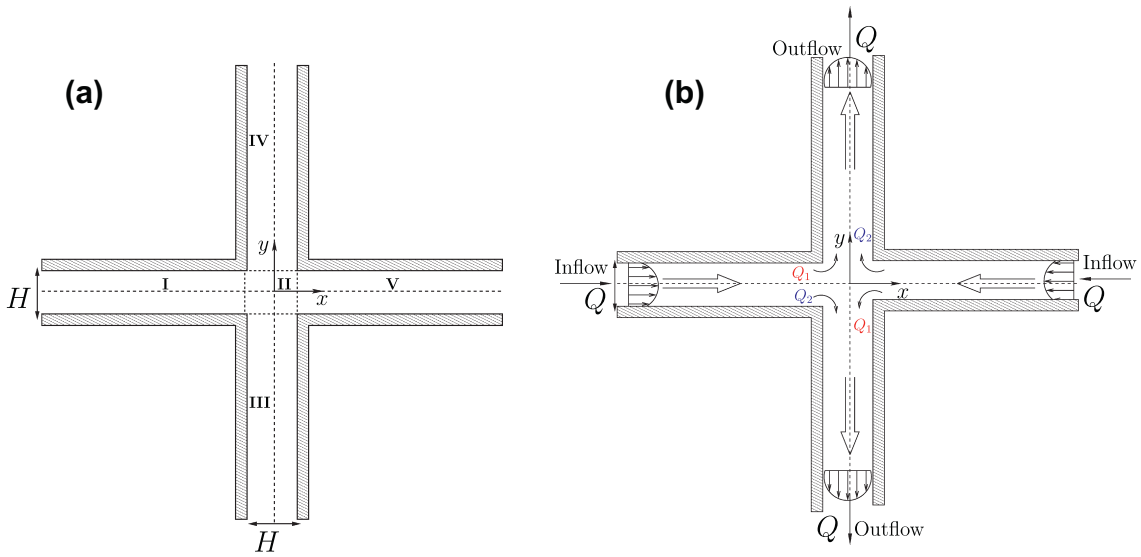

Fig. 5. Cross-slot geometry: (a) Division of the flow domain in blocks I, II, III, IV and V. (b) Scheme of flow rates Q, Q_1 and Q_2.

Table 2
Number of cells employed in each block of meshes $M1$ and $M2$ (cross-slot).

Meshes/Blocks	I	II	III	IV	V
$M1(\delta h = 1/25)$	125×25	25×25	25×125	25×125	125×25
$M2(\delta h = 1/50)$	250×50	50×50	50×250	50×250	250×50

$$\frac{\psi^{(n+1)}}{\delta t} - \frac{2\beta}{Re}\left[\left(\frac{\partial^2\psi^{(n+1)}}{\partial y^2}\right)n_x^2 + \left(\frac{\partial^2\psi^{(n+1)}}{\partial x^2}\right)n_y^2 - 2\left(\frac{\partial^2\psi^{(n+1)}}{\partial x\partial y}\right)n_x n_y\right] = \frac{2\beta}{Re}\left[-\left(\frac{\partial\tilde{v}^{(n+1)}}{\partial y}\right)n_x^2 - \left(\frac{\partial\tilde{u}^{(n+1)}}{\partial x}\right)n_y^2 + \left(\frac{\partial\tilde{u}^{(n+1)}}{\partial y} + \frac{\partial\tilde{v}^{(n+1)}}{\partial x}\right)n_x n_y\right] + \left[(\tilde{\tau}^{xx})^{(n+1)}n_x^2 + 2(\tilde{\tau}^{xy})^{(n+1)}n_x n_y + (\tilde{\tau}^{yy})^{(n+1)}n_y^2\right] - p^{(n)}. \quad (16)$$

The combination of Eqs. (15) and (16) leads to a large non-symmetric linear system which can be solved efficiently by the bi-conjugate gradient method (see in [22]).

Step 4: Compute the final velocity field from equation:

$$\mathbf{u}^{(n+1)} = \tilde{\mathbf{u}}^{(n+1)} - \nabla\psi^{(n+1)}, \quad (17)$$

which is deduced from the projection method [22].

Step 5: Compute the final pressure field by solving the following equation:

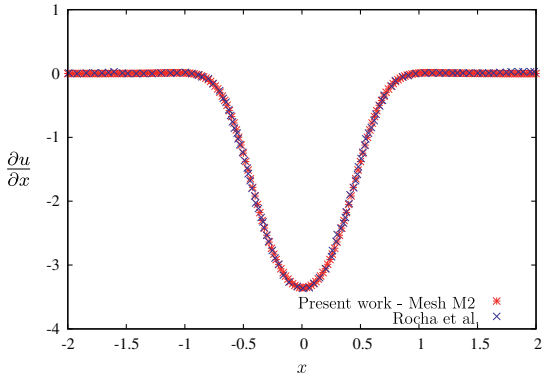

Fig. 6. Velocity gradient profile for Newtonian fluid flow along the centerline $-2 \leqslant x \leqslant 2,\ y = 0$. Comparison between our numerical solution and the results presented in [14].

$$p^{(n+1)} = p^{(n)} + \frac{\psi^{(n+1)}}{\delta t}. \quad (18)$$

Step 6: Calculate the final tensors $\mathbf{A}^{(n+1)}$ and $\boldsymbol{\tau}^{(n+1)}$. In the second stage of the RK21 scheme, the final conformation tensor $\mathbf{A}^{(n+1)}$ is obtained by solving

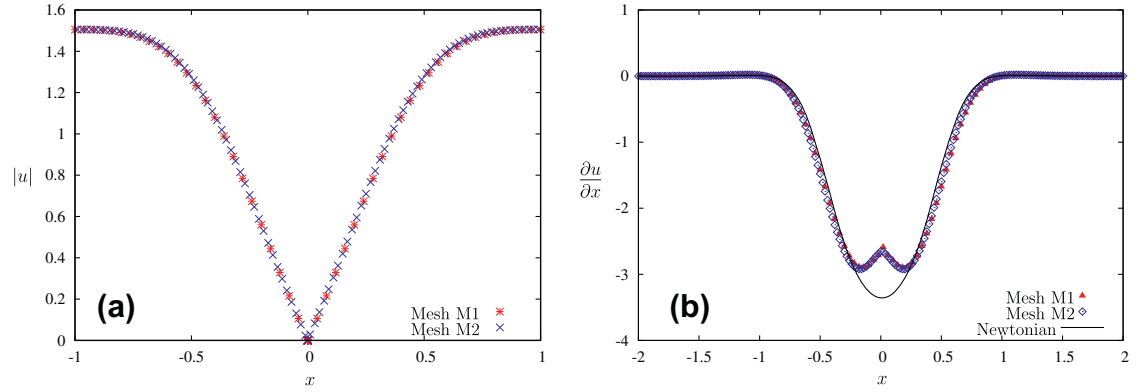

Fig. 7. Numerical simulation of cross-slot flow of a FENE-CR fluid with $Re = 0.01, Wi = 0.2, L^2 = 200$ and $\beta = 0.1$: (a) velocity profile $|u|$ for $-1 \leqslant x \leqslant +1,\ y = 0$ and (b) mesh refinement results of the profile of the velocity gradient along the centerline $-2 \leqslant x \leqslant +2,\ y = 0$.

Table 3
Bifurcation values obtained for the flow of a FENE-CR fluid in a cross-slot geometry with mesh $M2$ using $\beta = 0.1$ and $Re = 0.01$ for various values of Wi: column (a) $L^2 = 100$ and (b) $L^2 = 200$ (critical conditions are indicated in bold).

(a) $L^2 = 100$		(b) $L^2 = 200$	
Wi	$\|DQ\|$	Wi	$\|DQ\|$
0.00	0.000	0.00	0.000
0.35	0.001	0.30	0.000
0.40	0.007	0.38	0.059
0.41	0.028	0.39	**0.258**
0.42	**0.229**	0.40	0.378
0.43	0.351	0.41	0.462
0.455	0.526	0.45	0.663
0.46	0.551	0.50	0.787
0.60	0.839	0.60	0.894
0.70	0.894	0.70	0.934

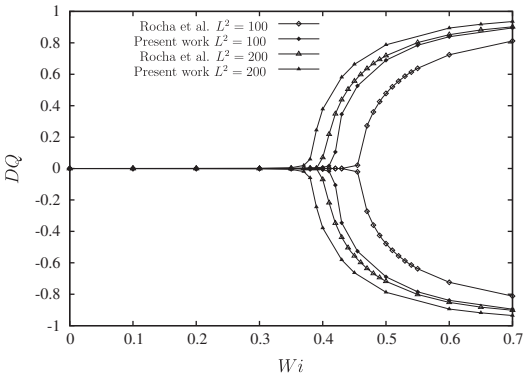

Fig. 8. Variation of asymmetry parameter DQ for different values of Wi: comparison with the results presented by Rocha et al. [14] for the FENE-CR model.

$$\mathbf{A}^{(n+1)} = \mathbf{A}^{(n)} + \frac{\delta t}{2}[\mathbf{F}(\mathbf{u}^{(n)}, \mathbf{A}^{(n)}) + \mathbf{F}(\mathbf{u}^{(n+1)}, \widetilde{\mathbf{A}}^{(n+1)})], \tag{19}$$

where $\widetilde{\mathbf{A}}^{(n+1)}$ has been calculated from Eq. (12). Finally, we can update the final values for the non-Newtonian tensor $\boldsymbol{\tau}^{(n+1)}$ using (3), namely,

$$\boldsymbol{\tau}^{(n+1)} = \frac{(1-\beta)}{ReWi} f(\mathrm{tr}(\mathbf{A}^{(n+1)}))[\mathbf{A}^{(n+1)} - \mathbf{I}]. \tag{20}$$

Step 7: Update the markers positions. The last step in the algorithm is to move the markers to their new positions. This is performed by solving

$$\frac{d\mathbf{x}}{dt} = \mathbf{u}, \tag{21}$$

for each particle using the second-order RK21 scheme that is described in detail in Oishi et al. [7].

3. Verification of the code: simulation of fully developed channel flow

To verify the correctness of the implementation of the numerical method proposed in this work, the filling of a two-dimensional channel (as shown in Fig. 1) was simulated. The simulation started with an empty channel. The fluid was injected at the entrance of the channel which was gradually filled. At the beginning, there was a moving free surface toward the channel exit.

At the channel entrance, the analytic profiles for the streamwise velocity $u(y)$ and the components of the conformation tensor $\mathbf{A}$ were imposed according to Eqs. (A.1), (A.4) and (A.6) (see Appendix A). The following data were used: $Re = 0.2$, $Wi = 0.4, \beta = 0.3$ and $L^2 = 100$. We simulated this problem using four uniform meshes: $M20 : 20 \times 200$ cells $(\delta h = 1/20), M30 : 30 \times 300$ cells $(\delta h = 1/30), M40 : 40 \times 400$ cells $(\delta h = 1/40)$ and $M50 : 50 \times 500$ cells $(\delta h = 1/50)$. To illustrate the behavior of the FENE-CR fluid in the

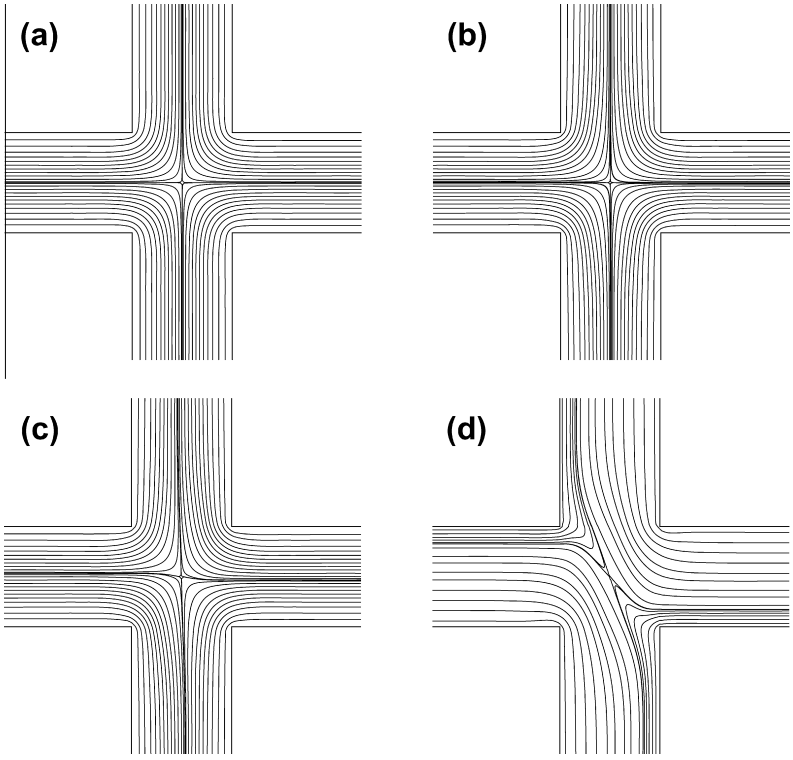

Fig. 9. Zoomed view of the streamlines in the cross-slot (mesh $M2$) for $Re = 0.01$ and various values of Wi: (a) Newtonian fluid, $Wi = 0$, (b) $Wi = 0.4$, (c) $Wi = 0.42$, and (d) $Wi = 0.6$. FENE-CR model with $L^2 = 100$ and $\beta = 0.1$.

Table 4
Definition of meshes $M3, M4$ and $M5$ (cross-slot).

Meshes/Blocks	I	II	III	IV	V
$M3, \delta h = 1/30$	150×30	30×30	30×150	30×150	150×30
$M4, \delta h = 1/40$	200×40	40×40	40×200	40×200	200×40
$M5, \delta h = 1/60$	300×60	60×60	60×300	60×300	300×60

channel flow problem, Fig. 2 displays the contours of the streamwise velocity u and of the components of the conformation tensor $\mathbf{A}$ at the dimensionless time $t = t^*(U/H) = 3.5$ obtained on mesh $M50$. We point out that at time $t = 3.5$ the channel is still being filled and the contours are not parallel which shows the transient state of the flow. At time $t = 50$, the channel is completely filled and the contour lines are all parallel indicating that steady state flow has been reached (not shown here for conciseness).

In order to assess the accuracy of our code, a convergence study for the variables u, A^{xx} and A^{xy} was performed at the middle of the channel $(x^* = 5H)$. The results obtained on the four meshes were compared with the corresponding analytic solutions. For clarity, only the results obtained on meshes $M30$ and $M50$ are displayed in Fig. 3 where it can be observed that the numerical solutions are in very good agreement with the analytic solutions.

The convergence of the numerical method was computed by using the Euclidean norms (l_2-norm) of the relative errors $(E(\cdot))$ between the analytic and numerical solutions on each mesh. The results displayed in Table 1 and Fig. 4 exhibit the variation of the errors with mesh size. It can be seen that the errors decrease with second-order accuracy (corresponding to the slope of the lines shown). These results confirm the second-order accuracy of the numerical method for solving the FENE-CR model for two-dimensional channel flows.

4. Numerical results for complex flows

In this section, the FENE-CR solver developed in this work is applied to investigate two-dimensional complex flows. Results obtained in the numerical simulation of the filling of the 2D cross-slot set-up by a FENE-CR fluid and the spreading of a FENE-CR droplet impacting on a rigid plate are presented. The meshes used in the following sections were uniform with spacing $\delta x = \delta y = \delta h$.

4.1. Planar cross-slot problem

The cross-slot flow is an important benchmark problem that has been used to investigate purely-elastic instabilities that can occur in low Reynolds number flows of viscoelastic fluids in two and three dimensions (see for example [11–14]). It is a configuration commonly employed when strong extensional flows are desirable such as in extensional viscosity measurements [25–27] and in single molecule studies [28], among other applications. Rocha et al. [14] provided quantitative numerical data for cross-slot flows of FENE-CR and FENE-P fluids in planar cross-slot geometries with sharp and rounded corners. They analysed the effects of finite extensibility, Weissenberg number and solvent viscosity ratio using a finite volume method.

In the present paper, we investigated whether the observed flow features reported by Rocha et al. [14] can be predicted by our finite difference method. To this purpose, we simulated the flow of FENE-CR fluids with a Newtonian solvent in a planar cross-slot geometry and compared our results with those obtained in [14]. We used $Re = 0.01$ (here chosen as $Re = \frac{\rho UH}{\eta_0}$ where H represents the width of the channel) and the flow domain employed in the computation is displayed in Fig. 5. In this geometry there are two opposite inflows and two opposite outflows, as shown in Fig. 5(b). On the inlets the analytic solutions for fully-developed flow for velocity and extra-stress components (see Eqs. (A.1), (A.4) and (A.6) in Appendix A) were imposed while on the outflows and rigid boundaries the conditions described in Section 2.1 were assumed. All channels had the same width H while for the channel lengths (represented by blocks I, III, IV, and V in Fig. 5(a)) the value $5H$ was used. The dimensions of the blocks shown in Fig. 5(a) are: Block I: $-5.5 \leqslant x \leqslant -0.5, -0.5 \leqslant y \leqslant 0.5$, Block II: $-0.5 \leqslant x, y \leqslant 0.5$, Block III: $-0.5 \leqslant x \leqslant 0.5, -5.5 \leqslant y \leqslant -0.5$, Block IV: $-0.5 \leqslant x \leqslant 0.5, 0.5 \leqslant y \leqslant 5.5$ and Block V: $0.5 \leqslant x \leqslant 5.5, -0.5 \leqslant y \leqslant 0.5$.

The meshes used to simulate this problem are detailed in Table 2.

We simulated first the cross-slot flow of a Newtonian fluid on meshes $M1$ and $M2$ (see Table 2) and Fig. 6 shows the good agreement between the predicted velocity gradient $\partial u/\partial x$ along the $y = 0$ centerline and the data of Rocha et al. [14].

For the FENE-CR model, we used the meshes $M1$ and $M2$ described in Table 2 to simulate the flow characterized by $Re = 0.01, Wi = 0.2, L^2 = 200, \beta = 0.1$. Fig. 7(a) displays the velocity profile $|u|$ for $-1 \leqslant x \leqslant 1$ and $y = 0$, while Fig. 7(b) shows the velocity gradient for $-2 \leqslant x \leqslant 2$ and $y = 0$. Good agreement between the solutions obtained on both meshes $M1$ and $M2$ is observed, demonstrating the numerical convergence of the results.

To supply additional results on this problem, we performed a quantitative comparison with the bifurcation data obtained by the FENE-CR solver developed in this work using mesh $M2$ and those presented by Rocha et al. [14] (see Table 3 and Fig. 8). The bifurcation variable is the flow rate imbalance DQ defined as $DQ = (Q_2 - Q_1)/Q$ where $Q = UH$ is the total flow rate per unit depth imposed at the two inlets which is split into the flow rates Q_1 and Q_2 at the center of the cross flowing in the direction of the upper and lower outlets (see Fig. 5b) [14]. If $DQ = 0$ then $Q_1 = Q_2$ which corresponds to a symmetric flow. Otherwise, if

Table 5
Bifurcation values ($|DQ|$) obtained for the flow of a FENE-CR fluid in a cross-slot geometry on meshes $M3$, $M4$ and $M5$ for $L^2 = 100$. For comparison, the results obtained on mesh $M2$ are also shown. Critical values are indicated in bold.

Wi	$M3$	$M4$	$M2$	$M5$
0.10	0.0006	0.0003	0.0001	0.0002
0.20	0.0006	0.0002	0.0001	0.0002
0.30	0.0006	0.0001	0.0007	0.0007
0.35	0.0006	0.0016	0.0018	0.0016
0.40	0.0006	0.0133	0.0076	0.0020
0.41	0.00055	0.0595	0.0280	0.0030
0.42	**0.2797**	**0.2447**	**0.2297**	**0.1994**
0.43	0.3765	0.3602	0.3511	0.3306
0.46	0.5541	0.5527	0.5511	0.5495
0.50	0.6834	0.6885	0.6893	0.6885
0.60	0.8287	0.8371	0.8390	0.8373

Table 6
Flow asymmetry values obtained on mesh $M2$ for the free surface flow of a FENE-CR fluid in a cross-slot geometry using $\beta = 0.1$, $Re = 0.01$ and various values of Wi for $L^2 = 100$ and $L^2 = 200$. Comparison with the results obtained in confined flows presented in Table 3.

(a) $L^2 = 100$			(b) $L^2 = 200$		
Wi	$\|DQ\|$-free surface	$\|DQ\|$-confined	Wi	$\|DQ\|$-free surface	$\|DQ\|$-confined
0.00	0.000	0.000	0.00	0.000	0.000
0.35	0.000	0.001	0.30	0.000	0.000
0.40	0.006	0.007	0.38	0.055	0.059
0.41	0.017	0.028	0.39	0.257	**0.258**
0.42	0.229	**0.229**	0.40	0.374	0.378
0.43	0.350	0.351	0.41	0.463	0.462
0.455	0.524	0.526	0.45	0.662	0.663
0.46	0.549	0.551	0.50	0.791	0.787
0.60	0.845	0.839	0.60	0.909	0.894
0.70	0.887	0.894	0.70	0.931	0.934

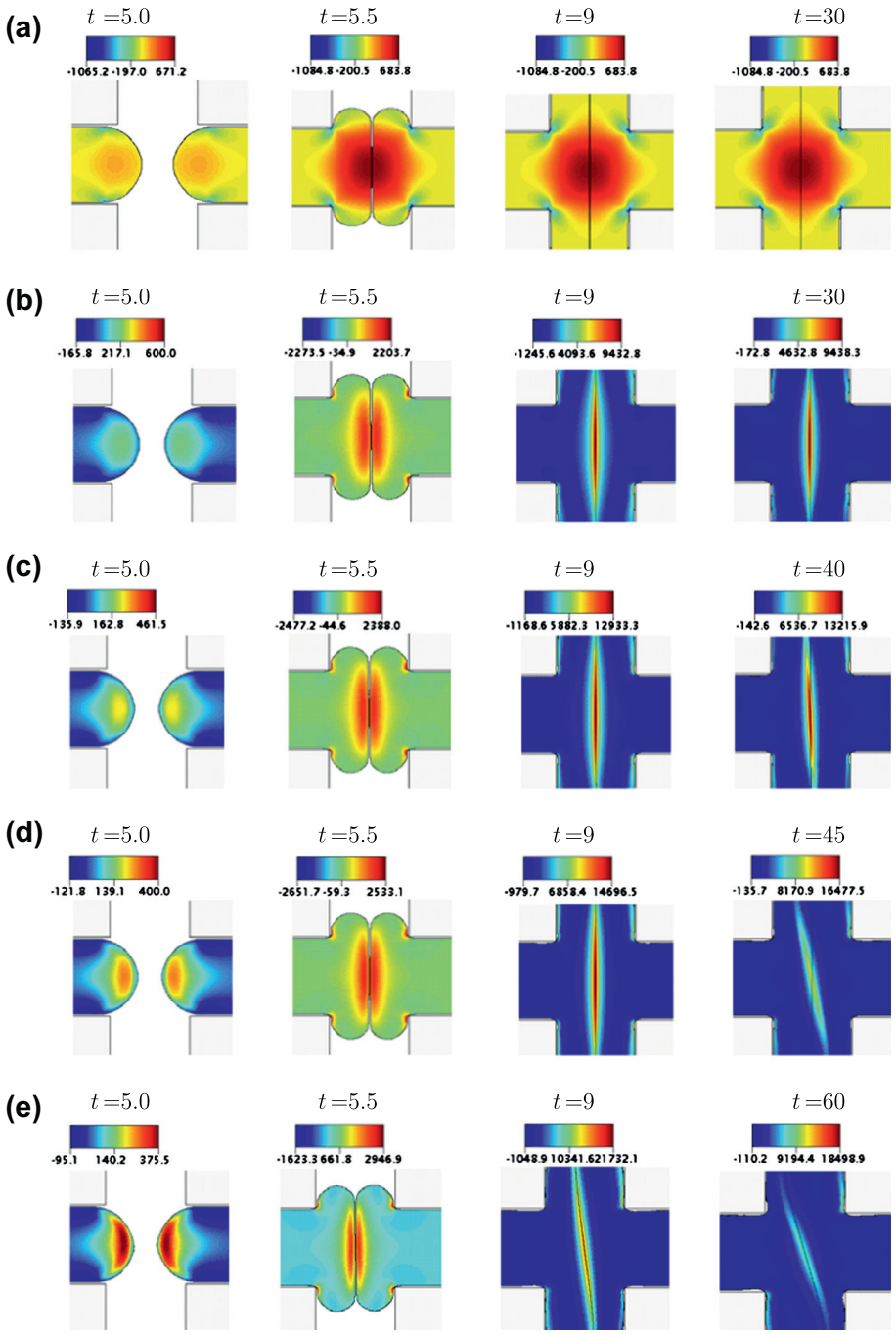

Fig. 10. Zoomed view of contour plots of τ^{yy} for FENE-CR fluids along time for: (a) Newtonian flows ($Wi = 0$), (b) $Wi = 0.3$, (c) $Wi = 0.39$, (d) $Wi = 0.45$, and (e) $Wi = 0.6$. There are moving free surfaces inside the cross-slot channels until $t \approx 10$.

$DQ > 0$ this implies that $Q_2 > Q_1$ which indicates more fluid coming from the left flowing down to the vertical channel. The maximum value for DQ is 1 ($Q_1 = 0$) and the minimum is $DQ = -1$ ($Q_2 = 0$). The results displayed in Table 3 and Fig. 8 show that the finite difference solver developed in this work is capable of capturing the first instability, where the steady flow transitions to a steady asymmetric flow. Although the bifurcation diagrams are qualitatively similar to those of Rocha et al. [14], there is a non-negligible difference in terms of the critical values. The present simulations were carried out on a uniform mesh, whereas those of Rocha et al. [14] were obtained by solving the governing equations using a finite volume method on a non-uniform mesh [14,30]. Specifically, in the present numerical methodology the asymmetry appears at smaller values of Wi ($Wi = 0.42$ for $L^2 = 100$ and $Wi = 0.39$ for $L^2 = 200$) than those obtained by Rocha et al. [14] ($Wi = 0.46$ for $L^2 = 100$ and $Wi = 0.41$ for $L^2 = 200$). With regard to $L^2 = 100$, Fig. 9 shows that the streamlines are symmetric for Wi up to 0.4 (see Fig. 9(a), Fig. 9(b)) while a small increase in the value of Wi (see Fig. 9(c)) causes the appearance of a small asymmetry and for $Wi = 0.6$ the flow is strongly asymmetric (see Fig. 9(d)).

4.2. Convergence study of the cross-slot flow through mesh refinement

To verify the convergence of the numerical method, the cross-slot problem was simulated on meshes $M3, M4$ and $M5$ defined in Table 4 and the critical values of Wi were calculated. The same input data used in Section 4.1 were employed. The results of these

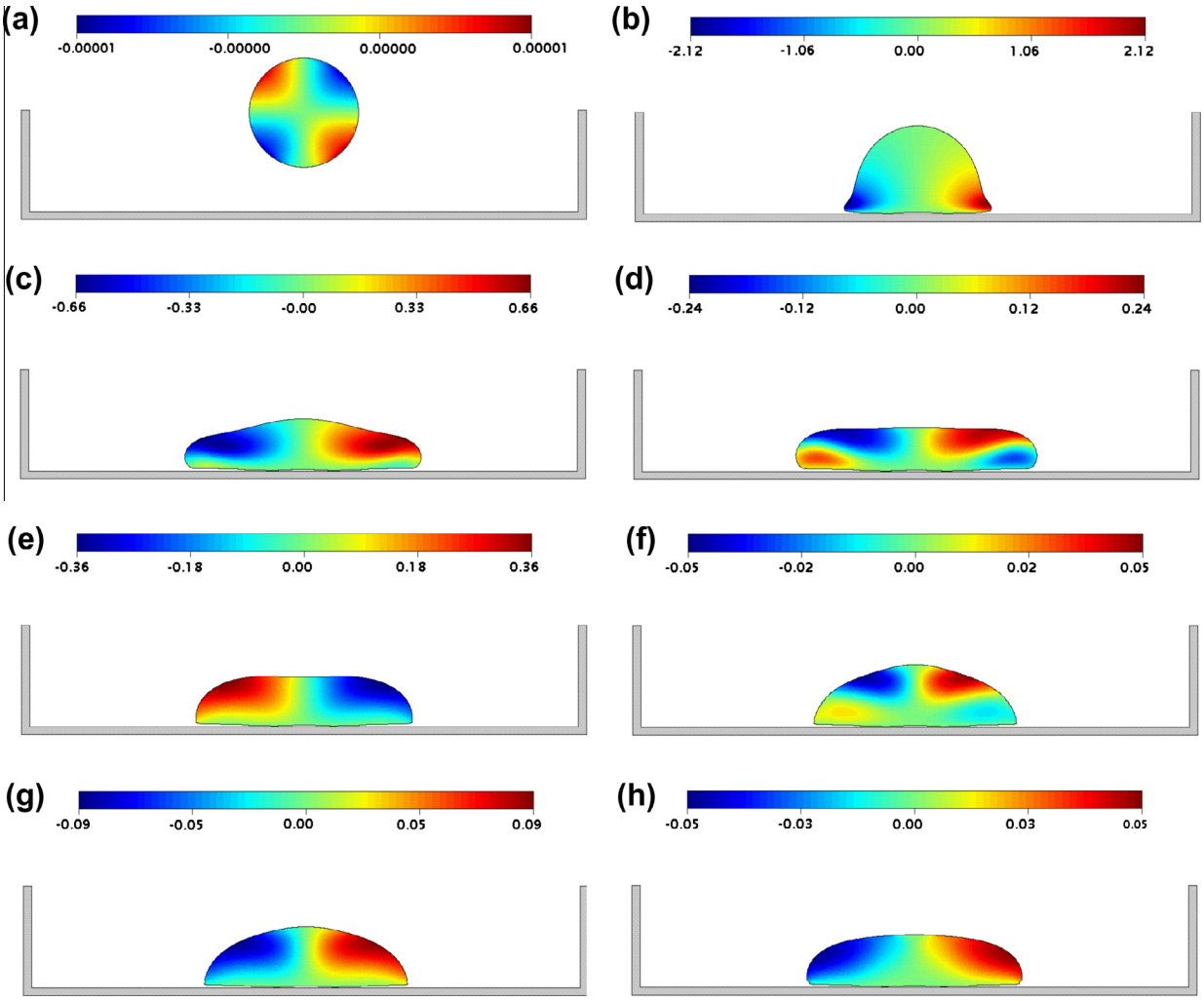

Fig. 11. Numerical simulation of the impacting drop problem using the FENE-CR model with $L^2 = 50$ ($Re = 5.0$; $Wi = 1.0$; $\beta = 0.1$; $Fr = 2.26$) on mesh $M2$. Illustration of the drop deformation and contours of the horizontal velocity for different dimensionless times: (a) $t = 1.0$, (b) $t = 1.5$, (c) $t = 2.0$, (d) $t = 2.3$, (e) $t = 3.0$, (f) $t = 3.8$, (g) $t = 4.0$, and (h) $t = 5.0$.

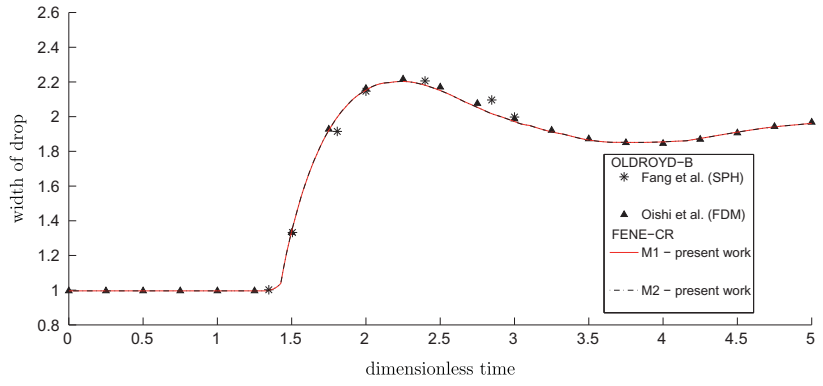

Fig. 12. Numerical predictions of the time evolution of the normalized width of the drop: comparison of FENE-CR model with $L^2 = 2000$ (present work) and the results obtained with an Oldroyd-B fluid ([3,7]) for $Fr = 2.26, Re = 5, Wi = 1.0$ and $\beta = 0.1$.

simulations are displayed in Table 5 where it can be seen that the critical values encountered are basically the same for all the meshes employed. These results confirm those obtained using meshes $M1$ and $M2$ presented in Table 3 and show the convergence of the numerical technique with mesh refinement applied to the cross-slot flow.

4.3. Numerical simulation of cross-slot flow with free surfaces

To demonstrate the ability of the finite difference code to simulate free surface flow instabilities, the cross-slot problem involving free surfaces was also investigated. The simulations started with an empty cross-slot domain. The fluid was injected through

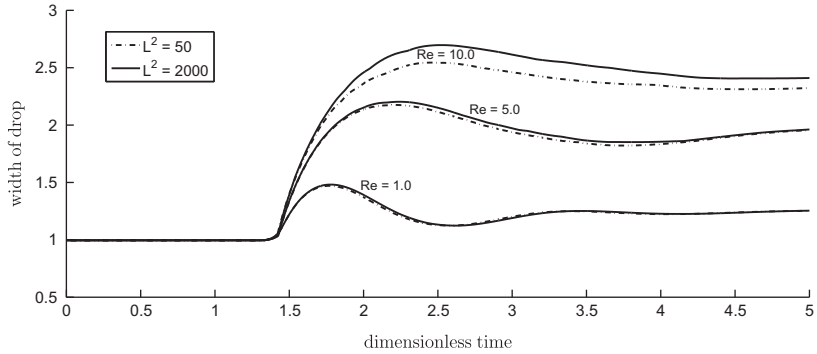

Fig. 13. Numerical simulation of drop impact with $Fr = 2.26$, $Wi = 1.0$ and $\beta = 0.1$ using mesh $M1$. Numerical predictions of the time evolution of the dimensionless width of a FENE-CR fluid drop: influence of Re and L^2.

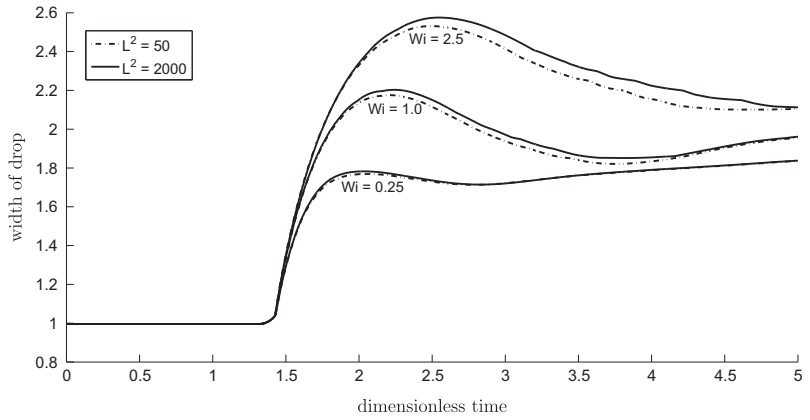

Fig. 14. Numerical simulation of drop impact with $Fr = 2.26$, $Re = 5.0$ and $\beta = 0.1$ using mesh $M1$. Numerical predictions of time evolution of the dimensionless of the width of a FENE-CR fluid drop: influence of Wi and L^2 on the drop width.

the two entrances, where the analytic solutions for fully developed flow were imposed, and the cross channels were progressively filled. At the front of the fluid, the boundary conditions imposed were the free surface stress conditions given by Eqs. (8) and (9). The input data used for simulating the free surface cross-slot flow of the FENE-CR fluid was the same data applied previously, namely, $Re = 0.01, \beta = 0.1$, $L^2 = \{100, 200\}$ and mesh $M2$.

In these simulations, the fluid crossed the outflows at approximately $t = 10$ and henceforth the cross-slot channels were completely full of fluid without any free surface. Table 6 displays the values of DQ after steady state has been established. It is seen that they are very close to those obtained in the computation of the fully confined flow. Thus, the computation of the filling process of the cross slot did not change the transitions found in the fully confined case in terms of the critical values of Wi and DQ.

These results are substantiated by Fig. 10 which displays contour plots of τ^{yy} for flows with $Wi = \{0, 0.3, 0.39, 0.45, 0.6\}$ and $L^2 = 200$. We can see that the Newtonian fluid flow and the FENE-CR viscoelastic fluid flow at $Wi = 0.3$ are symmetric; at $Wi = 0.39$ the flow starts becoming asymmetric and the asymmetry progressively increases with Wi. Even though the critical value of Wi and DQ are the same for the confined and free surface flow cases, there are some effects of the free surface on the transition process. For instance, for $Wi = 0.6$, the flow becomes asymmetric earlier in time than the flow with $Wi = 0.45$ (and 0.39) due to the different stress history at and around the stagnation point. Fig. 10 shows that at time $t = 9$, the flow corresponding to $Wi = 0.6$ is undergoing the elastic transition before the fluid exits the channel outlet whereas the lower Wi flow becomes asymmetric later when the fluid has gone through the outflow so that there is no free surface within the domain. These results are compatible with the requirement that the higher the value of Wi, the smaller the pertubation required to induce the instability.

To summarize, both the confined and free surface flows show the same flow transitions at essentially the same critical Wi value and for higher Wi the asymmetry of the filling channel anticipates in time the transition from symmetric to asymmetric flow relative to the fully confined case.

4.4. Impacting drop problem

In this section we consider the impacting drop problem. We analyse the time evolution of the shape of a drop of a FENE-CR liquid that is released from a distance H above a stationary plate.

We used the following data in the simulations: drop diameter $D = 2$ cm; initial velocity of the drop $U = 1.0\ \mathrm{ms}^{-1}$; clearance between released point and plate $H = 4$ cm and $g = -9.81\ \mathrm{ms}^{-2}$. We define the Reynolds number as $Re = \frac{\rho UD}{\eta_0}$ while the Weissenberg number is adopted as $Wi = \frac{U\lambda}{D}$. To demonstrate the convergence of the numerical method the impact drop problem was simulated using two meshes: mesh $M1$ with 156×156 cells ($\delta h = 0.025$) and mesh $M2$ with 312×312 cells ($\delta h = 0.0125$).

The time evolution of the flow produced by the FENE-CR drop is displayed in Fig. 11 where we can observe three stages of the drop evolution. The first stage starts after the drop impacted the plate and spreads out radially maintaining its concave shape (see Fig. 11(b)–(d)); the second stage begins at time $t = 3$ when, due to elastic forces, the sign of the horizontal velocity of the drop is inverted and the drop suffers a contraction and there is a formation of a dome (see Fig. 11(e) and (f)). The third stage occurred within

the dome shaped drop, where the horizontal velocity changes again its sign and the drop spreads radially (see Fig. 11(f)–(h)).

To compare with the results presented by Fang et al. [3] and Oishi et al. [7] who used the Oldroyd-B model, the following parameters were employed: $Fr = 2.26, Re = 5, Wi = 1.0,\ \beta = 0.1$. In the FENE-CR equation, we set $L^2 = 2000$ which is a sufficiently large value for the results obtained with the FENE-CR model to approximate those from the Oldroyd-B model. In these simulations, the dimensionless time-step used in meshes $M1$ and $M2$ were $\delta t = 2.0 \times 10^{-4}$ and 1.0×10^{-4}, respectively.

The variation of the dimensionless width of the viscoelastic fluid drop with the dimensionless time $t = t^* U/D$ is displayed in Fig. 12. For comparison, the results obtained by Fang et al. [3] and Oishi et al. [7] using the Oldroyd-B model are also shown in Fig. 12. The FENE-CR solutions approximate the Oldroyd-B results and agree very well with the data of Oishi et al. [7] and Fang et al. [3]. Moreover, the numerical solutions obtained on the two meshes are similar, which shows the convergence of the method with mesh refinement.

To provide further results on the impacting drop problem, we investigated the influence of the finite extensibility parameter and of the Reynolds number on the time evolution of the drop width. We employed mesh $M1$ and $Wi = 1, \beta = 0.1, Fr = 2.26$ and performed simulations using $Re = 0.1$, 1 and 5; for each value of the Reynolds number, simulations with $L^2 = 50$ and 2000 were carried out. The time evolution of the width of the drop is displayed in Fig. 13, where it can be seen that for $Re = 1$ and 5 the change in L^2 produced similar results, thus the effect of L^2 on the width of the drop is not too pronounced; however, at the higher $Re = 10$ case it is clearly more intense. The combined influences of L^2 and Wi were also investigated and the corresponding results are shown in Fig. 14 where it can be seen that for $Wi = 0.25$ the change in the value of L^2 did not cause significant variations in the width of the drop due to the small viscoelastic effect at such low Wi. However, as the Weissenberg number increases the effect of L^2 becomes more evident, as expected due to the increase in the viscoelastic behavior.

5. Conclusions

This work presented a finite difference technique for solving two-dimensional complex flows governed by the FENE-CR constitutive equation. The analytic solution for fully-developed channel flow was presented and employed to assess the convergence with mesh refinement and accuracy of the numerical method developed herein. The code was then applied to investigate fluid instabilities that can occur in cross-slot flows in the context of confined and free surface flows. The results obtained in these studies were compared with the finite volume predictions of Rocha et al. [14] and fair agreement between the two solutions was found. In spite of using a completely different numerical method, we predicted the same type of flow instabilities as Rocha et al. [14] and the difference with our critical Wi number was modest. To demonstrate that the numerical method developed in this work can deal with flows with complex moving free surfaces, the code was also applied to the simulation of the spreading of a drop impacting on a rigid plate. The time evolution of the drop width for a high value of L^2 was monitored and the results were compared with those given by Fang et al. [3] and Oishi et al. [7] for the Oldroyd-B model. Mesh refinement was employed and it was shown that, by using a large value for the extensibility parameter L^2, the FENE-CR solutions converged to the Oldroyd-B predictions of Oishi et al. [7]. The influence of the extensibility parameter L^2 on the spreading of the impact drop for different Reynolds and Weissenberg numbers was also examined, for $L^2 = 50$ and 2000. The results showed that for low Re and small Wi, the predictions of the drop width with $L^2 = 50$ and 2000 were similar. However, for higher Wi the changes in the width of the drop were more noticeable for varying L^2 values.

Acknowledgments

The authors acknowledge the financial support provided by the Brazilian funding agencies: FAPESP (Grants 2011/13930-0, 2009/15892-9), CNPq (Grants 472514/2011-3, 304422/2007-0, 470764/2007-4, 305447/2010-6). This research was initiated while the first author was visiting FEUP, Portugal, which was funded by PROPG/Unesp. This work is part of the activities developed within the CEPID-CeMEAI FAPESP project Grant No. 2013/07375-0 and also benefits from collaboration within the framework of the USP (Brazil) and UP (Portugal) research agreement and funding. M.A. Alves acknowledges funding from FCT, FEDER and COMPETE through project PTDC/EME-MFE/114322/2009.

Appendix A

Consider the shear flow of a FENE-CR fluid between parallel plates ($-0.5 \leqslant y \leqslant 0.5$), as illustrated in Fig. 1.

For fully-developed flow, the velocity profile is the same as for a Newtonian fluid due to the constant shear viscosity of the FENE-CR model:

$$u(y) = 1.5(1 - 4y^2). \tag{A.1}$$

The constitutive equation leads to the following variable components of the conformation tensor (note that $A^{yy} = A^{zz} = 1$ and $A^{xz} = A^{yz} = 0$),

$$2Wi\frac{du}{dy}A^{xy} = f(\mathrm{tr}(\mathbf{A}))[A^{xx} - 1], \tag{A.2}$$

$$Wi\frac{du}{dy} = f(\mathrm{tr}(\mathbf{A}))A^{xy}. \tag{A.3}$$

From Eq. (A.1) we obtain the profile of the velocity gradient, $\frac{du}{dy} = -12y$. The ratio between Eqs. (A.2) and (A.3) allow us to obtain the following relation involving A^{xx} and A^{xy}:

$$A^{xx} = 1 + 2(A^{xy})^2, \tag{A.4}$$

which can be substituted in Eq. (A.3) to yield

$$-12Wi\ y = \frac{L^2}{L^2 - 3 - 2(A^{xy})^2}A^{xy}. \tag{A.5}$$

This quadratic equation can be easily solved to obtain the fully-developed transverse profile of A^{xy}:

$$A^{xy} = \frac{L^2 - \sqrt{L^4 + 1152(L^2 - 3)Wi^2y^2}}{48Wi\ y}. \tag{A.6}$$

The A^{xx} component is now easily computed from Eq. (A.4). A similar derivation based on the non-Newtonian stress tensor was presented earlier in [29].

References

[1] T. Jiang, J. Ouyang, L. Zhang, X. Li, Improved SPH approach to branched polymer free surface flows based on the XPP model, Polym.-Plast. Technol. 50 (2011) 203–215.
[2] M. Tomé, N. Mangiavacchi, J.A. Cuminato, A. Castelo, S. McKee, A finite difference technique for simulating unsteady viscoelastic free surface flows, J. Non-Newt. Fluid Mech. 106 (2002) 61–106.
[3] J. Fang, R.G. Owens, L. Tacher, A. Parriaux, A numerical study of the SPH method for simulating transient viscoelastic free surface flows, J. Non-Newt. Fluid Mech. 139 (2006) 68–84.
[4] J.L. Favero, A.R. Secchi, N.S.M. Cardozo, H. Jasak, Viscoelastic flow analysis using the software OpenFOAM and differential constitutive equations, J. Non-Newt. Fluid Mech. 165 (2006) 1625–1636.

[5] B. Puangkird, F. Belblidia, M.F. Webster, Numerical simulation of viscoelastic fluids in cross-slot devices, J. Non-Newt. Fluid Mech. 162 (2009) 1–20.
[6] A. Rafiee, M.T. Manzari, M. Hosseini, An incompressible SPH method for simulation of unsteady viscoelastic free-surface flows, Int. J. Nonlin. Mech. 42 (2007) 1210–1223.
[7] C.M. Oishi, F.P. Martins, M.F. Tomé, M.A. Alves, Numerical simulation of drop impact and jet buckling problems using the eXtended Pom–Pom model, J. Non-Newt. Fluid Mech. 169-170 (2012) 91–103.
[8] T. Jiang, J. Ouyang, B. Yang, J. Ren, The SPH method for simulating a viscoelastic drop impact and spreading on an inclined plate, Comput. Mech. 45 (2010) 573–583.
[9] M.F. Tomé, G.S. Paulo, F.T. Pinho, M.A. Alves, Numerical solution of the PTT constitutive equation for unsteady three-dimensional free surface flows, J. Non-Newt. Fluid Mech. 165 (2010) 247–262.
[10] M.F. Tomé, A. Castelo, A.M. Afonso, M.A. Alves, F.T. Pinho, Application of the log-conformation tensor to three-dimensional time-dependent viscoelastic flows, J. Non-Newt. Fluid Mech. 175–176 (2012) 44–54.
[11] A.M. Afonso, M.A. Alves, F.T. Pinho, Purely elastic instabilities in three-dimensional cross-slot geometries, J. Non-Newt. Fluid Mech. 165 (2010) 743–751.
[12] M.S.N. Oliveira, F.T. Pinho, R.J. Poole, P.J. Oliveira, M.A. Alves, Purely elastic flow asymmetries in flow-focusing devices, J. Non-Newt. Fluid Mech. 160 (2009) 31–39.
[13] R.J. Poole, M.A. Alves, P.J. Oliveira, Purely elastic flow asymmetries, Phys. Rev. Lett. 99 (2007) 164503.
[14] G.N. Rocha, R.J. Poole, M.A. Alves, P.J. Oliveira, On extensibility effects in the cross-slot flow bifurcation, J. Non-Newt. Fluid Mech. 156 (2009) 58–69.
[15] M.A. Alves, F.T. Pinho, P.J. Oliveira, Study of steady pipe and channel flows of a single-mode Phan–Thien–Tanner fluid, J. Non-Newt. Fluid Mech. 101 (2001) 55–76.
[16] P.J. Oliveira, F.T. Pinho, Analytical solution for fully developed channel and pipe flow of Phan–Thien–Tanner fluids, J. Fluid Mech. 387 (1999) 271–280.
[17] D.O.A. Cruz, F.T. Pinho, Analytical solutions for fully developed laminar flow of some viscoelastic liquids with a Newtonian solvent contribution, J. Non-Newt. Fluid Mech. 132 (2005) 28–35.
[18] K. Gardner, E.R. Pike, M.J. Miles, A. Keller, K. Tanaka, Photon-correlation velocimetry of polystyrene solutions in extensional flow fields, Polymer 23 (1982) 1435–1442.
[19] P.E. Arratia, C.C. Thomas, J.D. Diorio, J.P. Gollub, Elastic instabilities of polymer solutions in extensional flows, Phys. Rev. Lett. 96 (2006) 144502.
[20] H.J. Wilson, Open mathematical problems regarding non-Newtonian fluids, Nonlinearity 25 (2012) R45–R51.
[21] G.K. Batchelor, An Introduction of Fluid Dynamics, Cambridge University Press, Cambridge, 1967.
[22] C.M. Oishi, F.P. Martins, M.F. Tomé, J.A. Cuminato, S. McKee, Numerical solution of the eXtended Pom–Pom model for viscoelastic free surface flows, J. Non-Newt. Fluid Mech. 166 (2011) 165–179.
[23] M.F. Tomé, S. McKee, GENSMAC: a computational marker-and-cell method for free surface flows in general domains, J. Comput. Phys. 110 (1994) 171–186.
[24] M.F. Tomé, B. Duffy, S. McKee, A finite difference technique for solving unsteady non-Newtonian free surface flows, J. Non-Newt. Fluid Mech. 62 (1996) 9–34.
[25] J.A. Odell, S.A. Carrington, Extensional flow oscillatory rheometry, J. Non-Newt. Fluid Mech. 137 (2006) 110–120.
[26] F.J. Galindo-Rosales, M.A. Alves, M.S.N. Oliveira, Microdevices for extensional rheometry of low viscosity elastic liquids: a review, Microfluid. Nanofluid. 14 (2013) 1–19.
[27] S.J. Haward, M.S.N. Oliveira, M.A. Alves, G.H. McKinley, Optimized cross-slot flow geometry for microfluidic extensional rheometry, Phys. Rev. Lett. 109 (2012) 128301.
[28] T.T. Perkins, D.E. Smith, S. Chu, Single polymer dynamics in an elongational flow, Science 276 (1997) 2016–2021.
[29] P.J. Oliveira, Asymmetric flows of viscoelastic fluids in symmetric planar expansion geometries, J. Non-Newt. Fluid Mech. 114 (2003) 33–63.
[30] P.J. Oliveira, Method for time-dependent simulations of viscoelastic flows: vortex shedding behind cylinder, J. Non-Newt. Fluid Mech. 101 (2001) 113–137.